AGU PUBLICATIONS

Radio Science

RESEARCH ARTICLE

10.1002/2014RS005529

Special Section:
URSI Symposium on Radiowave Propagation and Remote Sensing, 2013

Key Points:
- Describe the D3R as part of the GPM ground validation
- Provide a technical description of the D3R subsystems and calibration methods
- Characterize the performance of the D3R for remote sensing of precipitation

Correspondence to:
M. A. Vega,
Manuel.Vega@nasa.gov

Citation:
Vega, M. A., V. Chandrasekar, J. Carswell, R. M. Beauchamp, M. R. Schwaller, and C. Nguyen (2014), Salient features of the dual-frequency, dual-polarized, Doppler radar for remote sensing of precipitation, *Radio Sci.*, *49*, 1087–1105, doi:10.1002/2014RS005529.

Received 20 MAY 2014
Accepted 5 OCT 2014
Accepted article online 8 OCT 2014
Published online 18 NOV 2014

Salient features of the dual-frequency, dual-polarized, Doppler radar for remote sensing of precipitation

Manuel A. Vega[1,2], V. Chandrasekar[2], James Carswell[3], Robert M. Beauchamp[2], Mathew R. Schwaller[1], and Cuong Nguyen[2]

[1]NASA Goddard Space Flight Center, Greenbelt, Maryland, USA, [2]Electrical and Computer Engineering Department, Colorado State University, Fort Collins, Colorado, USA, [3]Remote Sensing Solutions, Barnstable, Massachusetts, USA

Abstract The global precipitation measurement (GPM) mission is an international satellite mission to obtain accurate observations of precipitation on a global scale every 3 h. Its (GPM) core satellite was launched on 27 February 2014 with two science instruments: the microwave imager and the dual-frequency precipitation radar. Ground validation is an integral part of the GPM mission where instruments are deployed to complement and correlate with spacecraft instruments. The dual-frequency, dual-polarization, Doppler radar (D3R) is a critical ground validation instrument that was developed for the GPM program. This paper describes the salient features of the D3R in the context of the GPM ground validation mission. The engineering and architectural overview of the radar is described, and observations from successful GPM ground validation field experiments are presented.

1. Introduction

Characterization of the space-time variability of precipitation at a global scale plays a vital role in understanding the impacts of climate change in the global energy and water cycle [*Hou et al.*, 2008]. The Global Precipitation Measurement (GPM) mission is an international partnership aimed primarily at two objectives, (1) the advancement in knowledge of the global water cycle and (2) the improvement of weather, climate, and hydrological prediction capabilities through more accurate and frequent measurements of global precipitation. Based on the success of the Tropical Rain fall Measuring Mission, the GPM core satellite carries a Ku-band weather radar with the addition of a Ka-band radar. The Ka-band radar provides higher sensitivity than the Ku-band radar and is useful for measurement of snow and light rain.

The GPM dual-wavelength retrieval methods will be used to characterize two parameters of the raindrop size distribution. Having a similar dual-wavelength radar on the ground with the potential for in situ and coordinated observations provides an excellent opportunity to develop microphysical models for microphysical retrievals. There are several assumptions used in the algorithms involving dual-wavelength methodologies discussed in the literature [*Seto et al.*, 2013; *Le and Chandrasekar*, 2014; *Meneghini et al.*, 1992]; therefore, a beam-aligned dual-wavelength system consisting of Ku and Ka bands will be very useful as a validation tool. In addition, if this system can be dual-polarized, the radar can be a self-consistent cross-validation tool.

The considerations and specifications of a ground-based dual-wavelength system are completely different from that of a space-borne system. In order for the space-borne dual-frequency retrieval to be successful, we need to understand the interaction between the microphysics and electromagnetics that generate the space-borne radar observations. The dual-polarization capability will enable additional microphysical insight into the interpretation of the dual-frequency observations seen by the space-borne radar. Doppler observations are also becoming an increasingly integral part of microphysical interpretation [*Moisseev and Chandrasekar*, 2007]. Thus, the above discussion points toward a dual-frequency, dual-polarized, Doppler radar as the best candidate for ground validation (GV).

The dual-frequency, dual-polarized Doppler radar (D3R) was jointly developed by NASA Goddard Space Flight Center, Colorado State University, and Remote Sensing Solutions. This paper describes the salient features of the D3R developed for the NASA GPM-GV program. The paper is organized as follows: Section 2 describes the architecture of the radar designed with the goal of participation in field deployments. Section 3 describes the subsystems of the D3R, namely the antenna subsystems, digital receiver, control and

©2014. American Geophysical Union. All Rights Reserved.

Figure 1. D3R system deployed in North Carolina for the Integrated Precipitation and Hydrology Experiment GPM-GV field campaign.

data processing, and the user interface. Calibration is an integral part of any radar system and those aspects of the D3R are described in section 4. Finally, sample results from field deployments are shown in section 5.

2. System Architecture

Since the GPM core satellite will be sampling precipitation at high latitudes, GPM-GV instrumentation is expected to be operational during field experiments spanning a wide range of environmental regimes with temperatures ranging from −40°C to 40°C and wind loads up to 25 m/s. Furthermore, ground instruments need to survive the perils of being assembled and disassembled in less than ideal scenarios involving unexpected weather conditions, utility power loss, and high winds, just to name a few.

A combination of requirements such as widely varying operational temperatures, ease of deployment, and ability to control remotely resulted in a decision to develop the radar using solid-state transmitters. Due to the comparatively low peak power output of solid-state transmitters as opposed to a magnetron or klystron, the radar system requires the use of pulse compression schemes to support the sensitivity requirement. Precipitation radar systems using solid-state transmitters are becoming increasingly viable [*Li et al.*, 2011; *Bharadwaj and Chandrasekar*, 2012]. Rapid strides made in semiconductor technology in the recent past have enabled the development of solid-state power amplifiers with sufficient power levels to serve as radar transmitters.

For a field deployable radar system, the solid-state transmitter solution offers several advantages including: no hot cathodes which eliminates warm-up time, lower system operating voltages, and improved mean time between failures. More recently, a class of frequency diverse wideband waveforms were developed to mitigate the low peak power of solid-state transmitters as well as the range blind zone problem associated with pulse compression [*Mudukutore et al.*, 1998; *Carswell et al.*, 2008; *Bharadwaj and Chandrasekar*, 2012].

The D3R employs a frequency-diversity waveform consisting of three frequency spaced subpulses to achieve its sensitivity and minimum range. The three pulses and their associated pulse duration are long (40 μs), medium (20 μs), and short (1 μs). The long and medium pulses are nonlinear frequency-modulated signals with an overall signal bandwidth of 3.6 MHz. The D3R frequency-diversity waveforms have a restriction requirement on the transmit waveforms' spectra to avoid overlapping of the subpulse frequency bands. The digital receiver filter utilizes a minimum integrated sidelobe level (ISL) filter which has been shown to be excellent for weather radar applications [*Bharadwaj and Chandrasekar*, 2012]. In the D3R system, minimum ISL filters are used for both long and medium pulses.

The D3R system, shown in Figure 1, was designed around the needs of the GPM-GV program. The radar system consists of two synchronized and coaligned radar (one Ku and one Ka) integrated on a common positioning system mounted on a flatbed trailer. The technical specifications of the D3R are summarized in Table 1. Both radar systems are dual-polarized and equipped with independent solid-state transmitters and receivers to allow for polarization diverse transmission schemes. The antenna system is composed of two prime focus antennas that are coaligned and possess well-matched beamwidths. The antennas are mounted on an aluminum frame designed to keep angular deflections to within 0.1° in any plane. The frame integrates both antennas, the RF transceivers, and IF analog/digital electronics onto the positioning system which minimized front-end losses and simplified the integration of the slip-ring assembly. These elements comprise the rotating subsystems shown in Figure 2. The positioning system consists of an elevation over azimuth configuration with scanning coverage of 360° in azimuth and −0.5–90° in elevation. The elevation

©2014. American Geophysical Union. All Rights Reserved.

Table 1. Specifications of the Dual-Frequency, Dual-Polarized, Doppler Radar (D3R)

	System
Frequency	Ku: 13.91 GHz ± 25 MHz, Ka: 35.56 GHz ± 25 MHz
Minimum detectable signal	Ku: −8 dB*Z*, Ka: −3 dB*Z*. Noise equivalent at 15 km and 150 m range resolution
Operational range resolution	150 m (nominal)
Minimum operational range	450 m
Maximum operational range	39.75 km
Angular coverage	0°–360° azimuth, −0.5°–90° elevation (full hemisphere)
	Antenna
Parabolic reflector diameter	Ku: 1.83 m, Ka: 0.71 m.
Gain	Ku: 45.6 dBi, Ka: 44.3 dBi
Half-power beam width	Ku: 0.86°, Ka: 0.90°
Polarization	Dual linear simultaneous and alternate (H and V)
Maximum sidelobe level	∼ −25 dB
Cross-polarization isolation	< −30 dB (on axis)
Ka-Ku beam alignment	Within 0.1°
Scan capability	0°–24°/s azimuth, 0°–12°/s elevation
Scan types	PPI sector, RHI, surveillance, fixed, vertical pointing
	Transmitter/Receiver
Transmitter architecture	Solid state power amplifier modules
Peak power	Ku: 200 W, Ka: 40 W per H and V channel
Duty cycle	30% maximum
Receiver noise figure	Ku: 4.8, Ka: 6.3
Receiver dynamic range	∼ 90 dB
Clutter suppression	GMAP-TD
	Data Products
Standard products	Equivalent reflectivity factor (Z_h), Doppler velocity (Ku unambiguous: 26.97 m/s)
Dual-polarization products	Differential reflectivity (Z_{dr}), Differential propagation phase (ϕ_{dp}), Copolar correlation coefficient (ρ_{hv}), Linear depolarization ratio (LDR_h, LDR_v) (in alternate mode operation)
Data format	NetCDF

limitations are physically set by the D3R design constraints, whereas the positioner design allows for elevation range of 0–180°. The positioning system is equipped with two one-gigabit Ethernet connections as well as a 20A, 208–240 Volts alternating current (VAC) circuit used to communicate and transfer power to the rotating subsystems shown in Figure 2. The positioning system also provides six differential signal pairs for timing, control, and housekeeping and an RF rotary joint for GPS signals.

The nonrotating subsystems group, shown in Figure 2, is composed of four 1U servers, a 64 TB (raw capacity) redundant array of inexpensive disks (RAID) storage device, one gigabit network switch, uninterruptible power system (UPS), dehydrator, and a 14 kW propane-powered generator equipped with an automatic transfer switch. All servers, network switch, RAID storage, dehydrator, and UPS unit are housed in temperature-controlled enclosures. Dry air from the dehydrator unit is cycled through the positioning system and all boxes mounted on it to prevent condensation. System control tasks (e.g., on/off control, transmitter enable, digital I/Q time series acquisition, and antenna control) are handled by the system control and data archiving node. Digital I/Q time series received from the digital receivers are disseminated to the signal processing and archiving nodes through the time series streaming server. The time series streaming server enables the processing and archiving of time series data simultaneously without exceeding the slip-ring data transfer bandwidth. Each radar has its own signal processing node that handles the generation and archiving of data products in real time. Real-time data products are then made available for display using the communication protocol defined for the VCHILL software [*Chandrasekar et al.*, 2005]. Any authorized internet-connected user can have access to real-time data by using the platform independent VCHILL display software. The UPS and generator provide automated backup of the entire system in the event of a loss of utility power. They also decouple the setup process from site preparations since the radar can be fully integrated and tested without the need for utility power, which has served us very well during deployments. The entire system is powered by a single 50 A, 208–240 VAC, 50–60 Hz circuit. Finally, the trailer is equipped with four outriggers with electric jacks used to level the platform and provide stability during high wind conditions.

©2014. American Geophysical Union. All Rights Reserved.

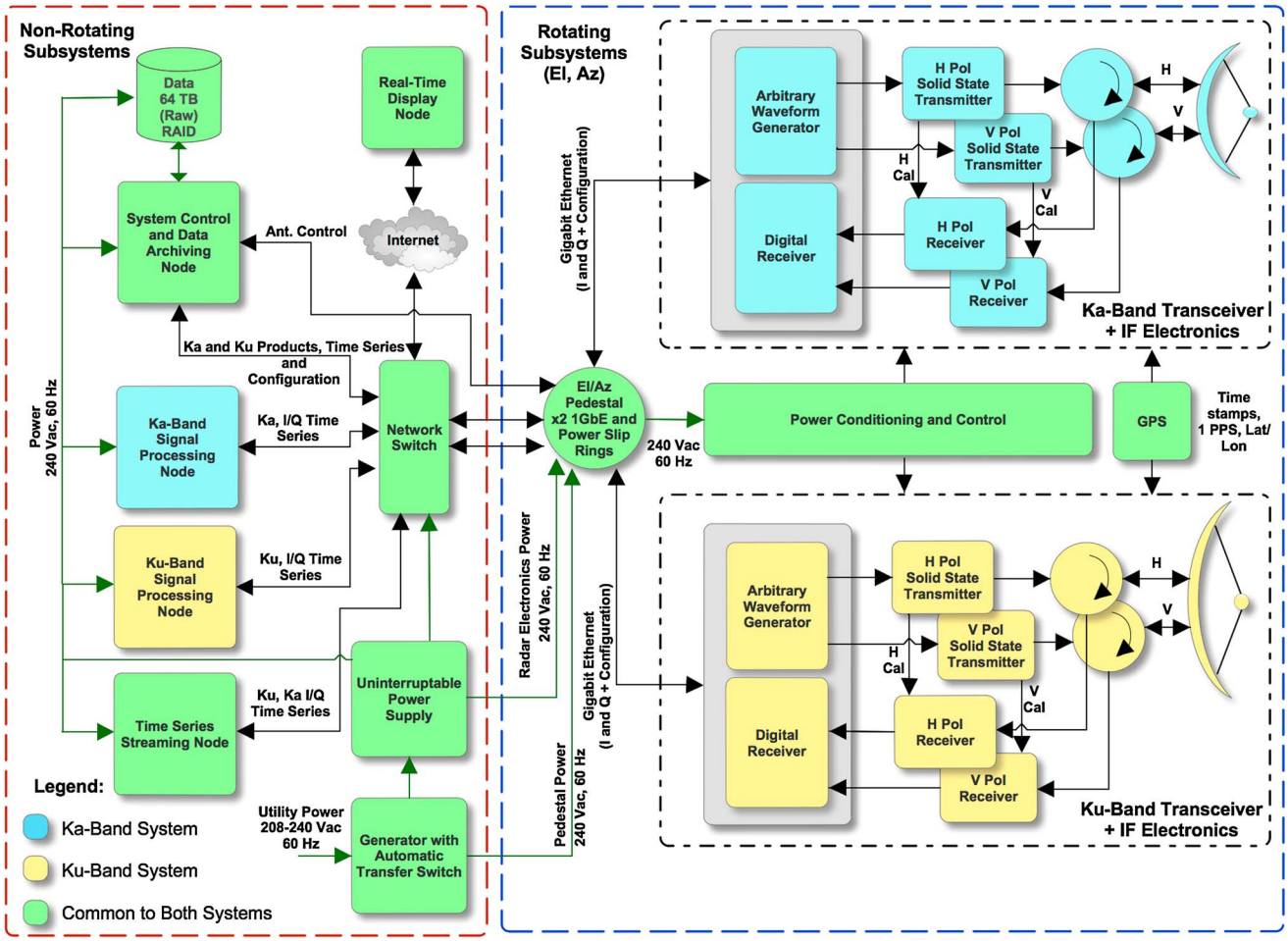

Figure 2. D3R system architecture diagram.

In preparation for shipment, the antennas and IF electronics box (rotating subsystems) are disassembled with the assistance of a forklift and stored in crates. Both antennas are kept integrated to the frame during shipment so that coalignment is maintained. The trailer can then be transported from site to site using a tow vehicle. The entire setup or teardown process is typically completed in 1 or 2 days.

3. D3R Subsystems

The D3R can be divided into three subsystems, namely (a) the antennas, (b) waveform and digital receiver subsystem, and (c) control and data processing system. The following subsections provide detailed descriptions of each of these subsystems.

3.1. Antennas

During the design phase, a dual-frequency, dual-polarized single aperture design was considered. However, estimated development cost and schedule at the time made it unfeasible. The antenna system employed on D3R consists of two dual linearly polarized prime focus parabolic reflector antennas. Four struts, each spaced 90° in the ϕ dimension hold the feed in place. Waveguides are routed from the feed to the back of the reflector along the 45 and 315° strut members. The feed was designed to hold 137.9-206.8 hPa (2–3 psi) of positive pressure, albeit our application does not require it due to the relatively low peak transmitter power. The reflectors are made of composite material, graphite over honeycomb, which makes them very lightweight and easy to handle when not integrated to the frame. To minimize the effects of wind loading, each antenna also includes an A-sandwich type radome. A hydrophobic coating is regularly applied to the radomes to prevent a water film from forming and therefore minimize attenuation effects as much as possible.

©2014. American Geophysical Union. All Rights Reserved.

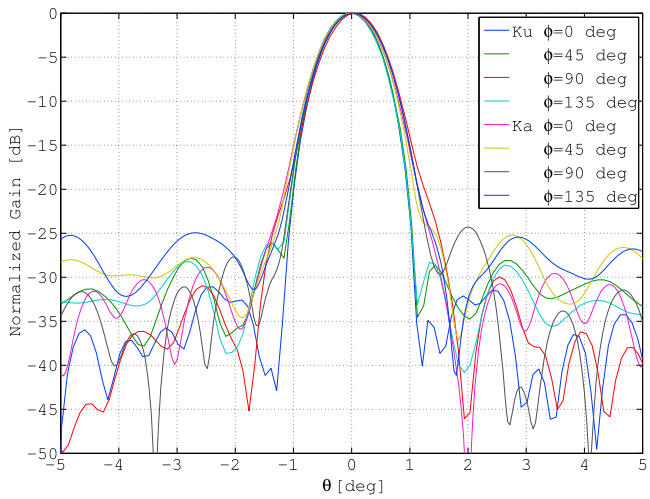

Figure 3. Ku, Ka-band H-port antenna copolarized power (normalized) antenna patterns.

Dual-frequency ratio, DFR, is the difference of the reflectivity, Z, at two different frequency bands. In the case of D3R, DFR is defined as $Z_{\mathrm{Ku}} - Z_{\mathrm{Ka}}$. Dual-frequency ratio is one of the variables measured by the D3R system and special consideration was given to the beam-matching and coalignment of the antennas. Figure 3 shows that the Ku and Ka bands overlaid H-port copolarized antenna patterns. The half-power beam widths for the Ku- and Ka-band antennas are on average 0.86 and 0.90°, respectively. This sets the azimuthal resolution at 30 km to approximately 470 m, which satisfied the requirement of it being $\leq$ 500 m. Overall, the Ku and Ka, peak sidelobe levels were below the required −25 dB level with the exception of the Ka $\phi = 90°$ plane which had its peak at approximately −24.3 dB. To achieve coalignment between antennas, provisions were made for four laser targets to be attached to the edges of both reflectors. The targets were used in combination with fine-resolution pattern measurements to derive beam offsets using a laser tracker. During integration of the antennas with the frame assembly, laser tracker measurements were used to determine beam coalignment and shims were strategically applied to the Ka-band antenna until the Ka matched the Ku-band beam pointing. The final result was a coalignment within 0.1° in both azimuth and elevation. Please refer to the section on calibration, section 4, for coalignment verification results.

In addition to DFR measurements, polarimetric measurements such as differential reflectivity (Z_{dr}), differential propagation phase (ϕ_{dp}), copolar correlation ($|\rho_{hv}|$), and linear depolarization ratio (LDR) are all part of the capabilities incorporated into the design. The quality of the polarimetric variables are dependent on the antenna's polarimetric performance. Copolarized H- and V-port pattern matching, cross-polarization isolation, and differential phase patterns are three parameters that have a significant effect on polarimetric variables [*Bringi and Chandrasekar*, 2001; *Wang et al.*, 2006; *Mudukutore et al.*, 1995]. Figures 4 and 5, Ku and Ka, respectively, show the copolarized and cross-polarized antenna pattern for the H and V ports in $\phi = 45$ and $\phi = 135°$ planes where feed strut blockage is present. Copolarized beam matching was evaluated by integrating the two-way pattern over the main lobes (null-to-null) for each port and computing the percent difference between ports. A maximum percent difference of the patterns of 3.63% for Ku band and −3.04% for Ka band was found. The two-way integrated (main lobe, null-to-null) cross-polarization isolation, ICPR_2 [*Chandrasekar and Keeler*, 1993] is given by

$$\mathrm{ICPR}_2 = 10\log_{10}\left[\frac{\int f_{co} f_{cx} \sin\theta \, d\theta}{\int f_{co}^2 \sin\theta \, d\theta}\right] \quad (1)$$

where f_{co} and f_{cx} are the normalized copolarized and cross-polarized antenna power patterns, respectively. The worst-case plane for cross-polarization power of the Ku-band antenna is shown in Figure 4. The worst-case cross-polarization

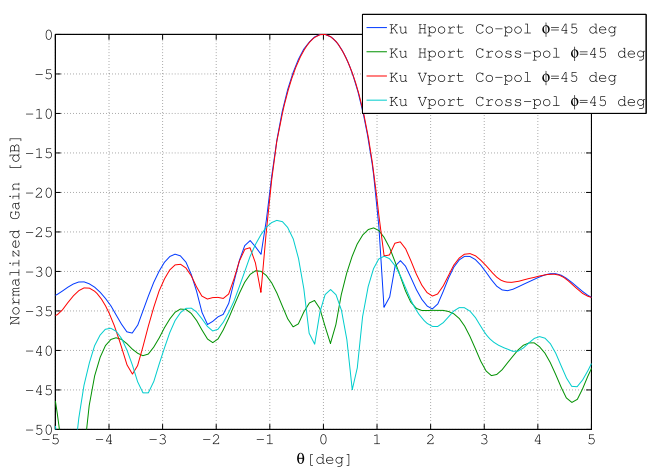

Figure 4. Ku-band H- and V-port antenna copolarized and cross-polarized power (normalized) antenna patterns for worst-case cross-polarization plane.

©2014. American Geophysical Union. All Rights Reserved.

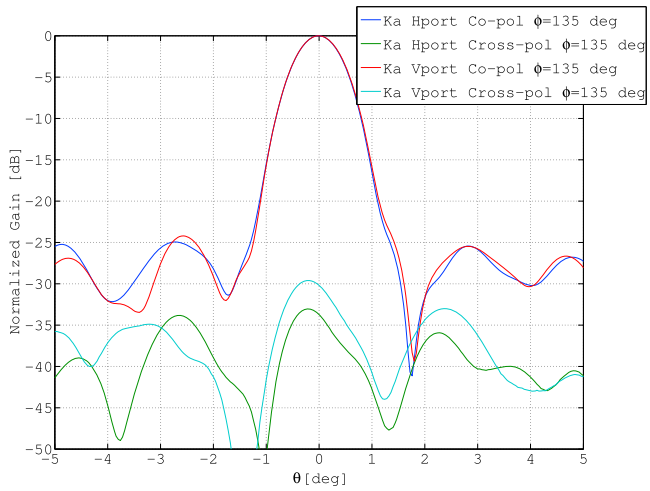

Figure 5. Ka-band H- and V-port antenna copolarized and cross-polarized power (normalized) antenna patterns for worst-case cross-polarization plane.

isolation is −29.13 dB for the H port and −29.19 dB for the V port. Similarly for the Ka-band antenna, Figure 5 shows the worst-case plane for cross-polarization isolation with −32.56 dB on the H port and −29.02 dB for the V port. Overall, the goal was to not exceed −32 dB cross-polarization isolation. However, after several adjustments and subsequent pattern measurements, both antennas were accepted as described.

3.2. Waveform Generation, Transceiver, and Digital Receiver Subsystems

Advances in the area of RF solid-state power amplifiers (SSPAs) coupled with increased logic density in field programmable gate array (FPGA) chips during the definition stage of the D3R presented the possibility of adopting such technologies in the design of the transmitter, digital signal synthesis, and digital signal processing subsystems. The use of pulse compression techniques becomes necessary in this type of design due to the low peak output power achieved with SSPAs in comparison to other classes of radar transmitters such as tube amplifiers, magnetrons, and klystrons. The SSPA solution provides wide bandwidth (in the context of weather radar) and allows for high operational duty cycles. This allows the possibility of using multiple frequency spaced and time multiplexed subpulses, including frequency-modulated pulses, that enable sensitivities and blind ranges comparable to those attained with other types of transmitters requiring the use of high-voltage electronics.

3.2.1. Signal Path Description

Figure 6 shows the transceiver architecture implemented in both the Ku- and Ka-band subsystems. To enable the measurement of all polarimetric scattering matrix elements, a dual-transmitter, dual-receiver configuration was adopted. Digitally synthesized transmit signals, centered at the first intermediate frequency (IF) of 140 MHz for each channel (H and V), are generated in the arbitrary waveform generator (AWG). Timing signals are also generated in the AWGs and will be discussed in more detail in the following section. The transmit waveform is stored as digital I/Q value pairs at baseband with a sample rate of 50 MHz for each channel. The transmit waveform is downloaded to the AWG's onboard memory via a USB interface using a single-board computer (SBC) which also hosts the digital receiver (DRX). The AWG uses quadrature digital up-converters (DUCs) with built-in 14-bit digital-to-analog converters to interpolate and translate the loaded baseband waveform to a center frequency of 140 MHz at a sample rate of 1 GHz. This stage is followed by IF section 1, which includes filtering, amplification, and mixing stages to convert the signal from the 140 MHz IF to the second IF of 220 MHz for Ku band and 920 MHz Ka band. The 360 MHz and 780 MHz signals used in the first and last mixing stages are generated by phase-locked coaxial resonator oscillators

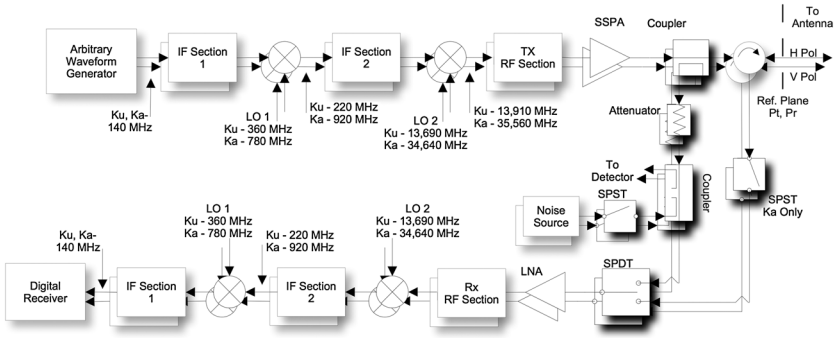

Figure 6. Ku, Ka-band transceiver architecture block diagram.

©2014. American Geophysical Union. All Rights Reserved.

combined with four-way splitters. IF stage 2 is followed by another set of filtering, amplification, and mixing stages arriving at the final operating frequencies of 13.91 GHz for Ku and 35.56 GHz for Ka. The transmitter RF section performs the final filtering stage, with preamplifier also included on Ka band, prior to entering the SSPAs. The mixing signal of 13.69 GHz on the Ku-band transceiver is generated from a phase-locked dielectric resonator oscillator, and the 34.64 GHz on the Ka band is generated from a 17.32 GHz oscillator of the same type which is then split four ways and fed into four frequency multipliers (× 2) with filtering stages prior to entering the mixers.

The front-end section of both transceivers contains the SSPAs, calibration path components, duplexer, and low-noise amplifier (LNA). The SSPAs peak output power for each polarization channel is approximately 200 W for the Ku band and approximately 40 W for the Ka band. Both sets of SSPAs are equipped with internal temperature compensation for gain and high-speed on/off switching. Temperature-compensated gain control prevents major drifts in system transmit power due to thermal cycling, and the high-speed on/off capability provides a means to shutdown the internal bias to all power modules after the transmit period is completed. This has two major advantages over an "always on" approach: (1) less power consumption and therefore less heat generation and (2) thermal noise leakage into the receiver during the receive mode is minimized without the need for additional high-power switches.

Once the transmit waveform is amplified by the SSPA, it is coupled into the receiver though a calibration channel which provides a means to track and compensate for gain drifts in the transmitter and receiver [*Durden et al.*, 1994; *McLinden et al.*, 2008; *Vega et al.*, 2012; *Ulaby et al.*, 2014]. The selection between the receiver and calibration path is performed through a single-pole double-throw (SPDT) switch implemented using PIN diodes on the Ku and latching circulators on the Ka. Since leakage through the circulator and reflections from the antenna ports will add coherently to the calibration signal, over 40 dB of isolation is needed between the calibration and leakage/reflection signals for a transmit power measurement corruption of less than 0.1 dB. On the Ku, the PIN diode-based SPDT provided enough isolation to meet the desired calibration-to-leakage ratio. On the Ka, an additional single-pole single-throw switch (also implemented using latching circulators) was added to meet the isolation requirements. An attenuator is used to set the sampled power level well below the receiver saturation point (approximately 75–80 dB of total calibration path attenuation) followed by another coupler with a square law detector which provides a quick and independent method to measure the transmitter power during system checks. A noise source with an excess noise ratio (ENR) of 27 dB for Ku and 22 dB for Ka is coupled into the receiver as well for independent receiver gain tracking. During a typical transmit/receive cycle, the SPDT switch is set to the calibration path, the noise source switch is closed for several μs followed by the enabling of the SSPAs, and triggering of the AWGs which results in the sampling of the transmitted waveform. The SSPAs are then disabled, and the SPDT is returned to the receive path. This process is repeated on a pulse-by-pulse basis.

Received signals are routed from the antenna to the receiving path where they are initially amplified by LNAs with approximate noise figures of 1.2 and 2.6 dB and gains of approximately 26 and 21 dB for Ku and Ka, respectively. The LNAs are followed by several component stages which are in common with the transmitter calibration loop until they reach the digital receivers.

The digital receivers employed are based on a Peripheral Component Interconnect (PCI) Mezzanine Card equipped with four (only two are used) 16-bit analog-to-digital converters (ADCs), signal-processing and PCI bridge FPGAs, and general purpose I/O. This card is hosted by a compact PCI single-board computer (SBC) housed in a 1U, 48.26 cm (19-inch) rack mountable chassis. Signals received from all three subpulses are digitized and divided into three subchannels where they are processed by quadrature downconversion stages, decimating filters, and ending in either matched filters or pulse compression filters. Digital I/Q data are then transferred from the DRX to the SBC via the PCI bus where it is tagged with GPS derived time stamps and location, antenna position, scan type, transmitter state, and other metadata required by the signal processing nodes.

3.2.2. Timing and Clock Interface Description

The Ku and Ka bands use a common 10 MHz stable local oscillator (STALO). The 10 MHz STALO clock source is used to generate the radio frequencies (RF), intermediate frequencies (IF), and the digital receiver ADC sampling clock. A diagram of the clock distribution is provided in Figure 7. A GPS module provides radar location information, UTC timestamp information, and a synchronization pulse at 1 pulse per second that is common to both the Ku- and Ka-band receivers. The arbitrary waveform generator (AWG) generates the

©2014. American Geophysical Union. All Rights Reserved.

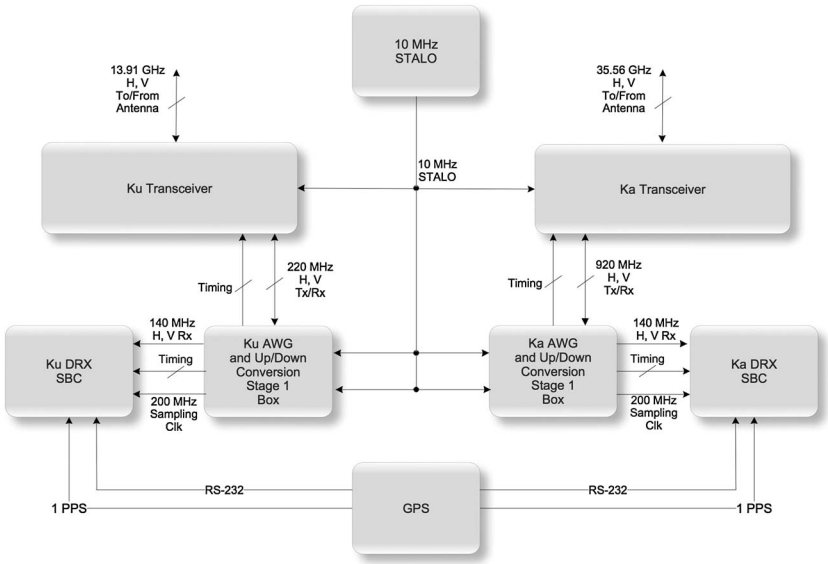

Figure 7. System timing and clock generation block diagram.

requisite triggers and timing delay for the transceivers and digital receiver (DRX). The precise timing from the AWG is used to coordinate the calibration sources within the transceiver, SSPA control, and the synthesis of transmit waveforms. The Ka AWG trigger is slave to the Ku AWG trigger to allow synchronized transmission and acquisition of both Ku and Ka radars.

3.3. Control and Data Processing System

The radar control and data processing can be subdivided into three subsystems: antenna control, RF control, and data processing. These three subsystems interact with one another and provide state information for data processing. The subsystems are integrated into a single point of control provided as a user interface. Antenna control is common for both Ku and Ka, while the RF control and data acquisition are logically separated for the Ku and Ka bands. Synchronous transmission of both frequencies is achieved by operating the Ka trigger generator as a slave device to the Ku trigger generator. All hardware devices are individually powered and remotely controlled through an Ethernet-enabled power distribution unit (PDU). The PDU provides power sequencing capability and remote fault recovery in the event of a system power issue. Due to the network-driven architecture, the D3R can be remotely operated, without limitation, via an Internet connection.

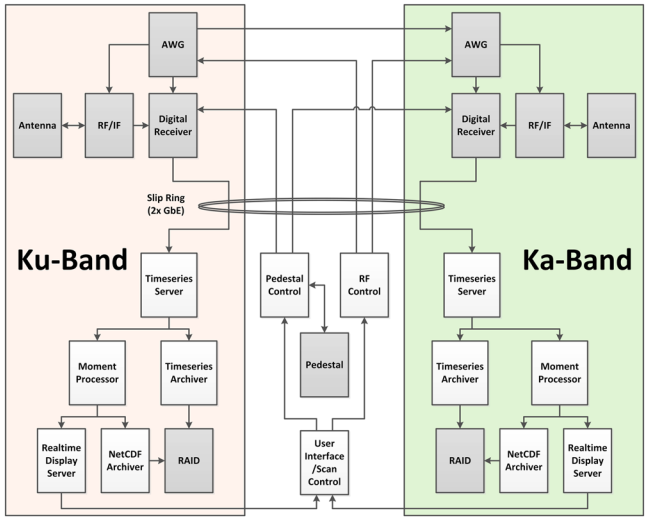

Figure 8. D3R software system diagram. Dark gray boxes represent hardware or firmware devices. Light gray boxes represent software modules running on general purpose servers.

In Figure 8, the IF box houses the common 10 MHz local oscillator, Ku- and Ka-band arbitrary waveform generators (AWGs), and Ku- and Ka-band digital receivers (DRXs). Both of the DRXs have dedicated gigabit Ethernet connections, via the pedestal slip ring, to their respective data processing servers. RF control and the housekeeping function share the gigabit Ethernet connections for control and monitoring of the system. The D3R system uses a redundant array of inexpensive disks (RAID) to provide both fault tolerance in the archiving of data and to meet the data bandwidth requirements for data archiving time series I/Q data. The RF/IF hardware is controlled by the

©2014. American Geophysical Union. All Rights Reserved.

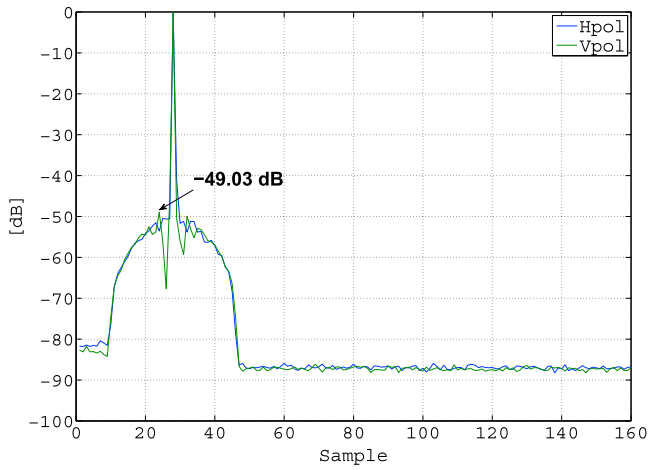

Figure 9. Ku-band pulse compression waveform and filter response for the medium pulse illustrating range sidelobes.

precise timing of the AWG. The AWG is responsible for all timing, triggers, and transmit waveform generation. The digital receiver is implemented with an FPGA acquisition board running on a Linux-based single-board computer. All movement of the radar system is controlled by the trailer-mounted pedestal.

3.3.1. Antenna Positioning

Antenna positioning is accomplished by controlling the pedestal. The pedestal is scanned by providing start and stop azimuth and elevation coordinates, direction of movement, and movement rate. The pedestal state can be queried to monitor the current position and status information. Complex scans can be generated by executing a sequence of move commands. The pedestal hardware provides a serial communication interface for all communications. A serial-to-Ethernet adapter is used to allow pedestal control to be managed from any networked computer. A dedicated service is run on a general purpose Linux server as the pedestal controller. The pedestal controller service provides a managed interface for all other servers or services to access the pedestal state and control the pedestal. This implementation allows for the arbitration of multiple clients to the pedestal resources.

3.3.2. RF Control

All RF control is enabled via the AWG. The AWG allows for detailed timing and trigger generation, the configuration of waveform input, pulse-by-pulse transmit phase control, pulse repetition period (PRT) timing, PRT mode selection, and enabling and disabling transmit triggers. With proper configuration of the AWG timing, various polarization states and PRT sequences are generated to enable any transmit polarization modes with either a uniform PRT or nonuniform PRT scheme, such as a staggered PRT waveform.

D3R operates with the Ku-band AWG as the master trigger source and the Ka-band AWG as a slave device that generates the Ka transmit trigger when the Ku-band trigger is generated. D3R's standard operating mode is simultaneous transmit and receive of both polarization channels, with 400 μs/600 μs staggered PRT. For uniform PRT, a 500 μs period is used.

3.3.3. Data Processing

As discussed previously, the D3R's digital receivers are implemented using an FPGA-based analog acquisition board hosted by a single-board computer running Linux. The digital receiver encodes the system status and position in the time series data structures it sends to the moment processor; however, the digital receiver does not use this data itself. The digital receiver also encodes information about the operating mode of the AWG, making information such as the polarization mode and PRT selection available to the moment processor to correctly process the digital I/Q data.

The data processing is performed using general purpose servers running the Linux operating system with proprietary radar data processing software. Gigabit Ethernet connections are used to share data between the digital receivers and processing servers. The data processing software is divided into functional modules with network-enabled interfaces for data transport. This allows the data processing to be balanced and distributed over multiple servers.

The FPGA-based digital receiver implements a multifrequency pulse compression design to allow the use of three independent, frequency-separated subpulses. The three center frequencies are separated by 15 MHz, with a 10 MHz channel bandwidth each. The typical range sidelobe level is illustrated by the pulse compression filters for the Ku medium pulse in Figure 9. It can be seen from this figure that the typical range sidelobe levels are of the order of −49 dB and they uniformly fall to less than −85 dB at further range delays. These three subpulses are designed to work together to maximize the radar's sensitivity while mitigating the blind range limitations inherent to pulse compression. The digital receiver acquisition board directly

©2014. American Geophysical Union. All Rights Reserved.

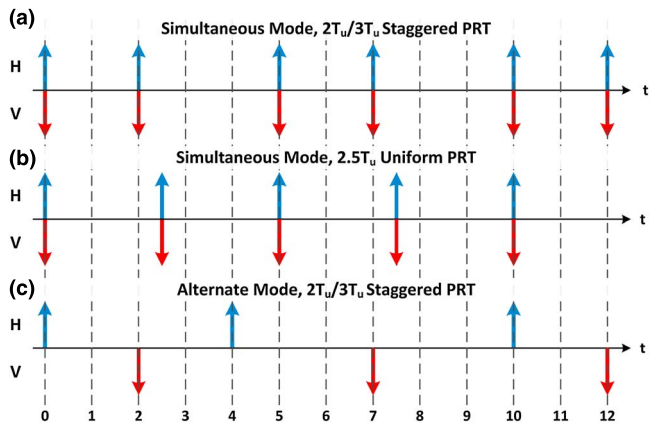

Figure 10. D3R pulse schemes for simultaneous mode with (a) both uniform PRT and (b) staggered two-thirds PRT. The uniform PRT and staggered two-thirds PRT waveforms yield the same effective sampling rate over a ray integration cycle. (c) The alternate mode staggered PRT pulse timing for D3R is illustrated.

samples the IF frequency and provides a time series data stream, which includes the radar state information and digital I/Q data of the three subpulses for the entire pulse acquisition time.

The digital receiver computer transfers the time series data via Ethernet through the pedestal slip ring to a time series server. The time series server is used as a first-in, first-out buffer between the digital receiver and all time series consumers. The time series server provides fan out of the time series data to maintain the minimum data bandwidth load through the pedestal slip ring, which presents a network bandwidth bottleneck. Any consuming software client that requires time series data can connect to the time series server without increasing the network load on the digital receiver. The moment processor and time series archiver are two consumers of the time series data stream.

The radar moment processor uses the Gaussian model adaptive processing in the time domain (GMAP-TD) clutter suppression algorithm [*Nguyen and Chandrasekar*, 2013] at its core. The main concept of the GMAP-TD method is to design a time-varying filter matrix to attenuate the clutter signal to a level comparable to the noise. The processing methodology is similar to the original GMAP filter [*Siggia and Passarelli*, 2004], but all processing is performed in the time domain. Therefore, it overcomes the disadvantages associated with spectral processing methods such as the effect of spectral leakage caused by finite data length and the effects of aggressive time domain weighting functions have on the estimation of signal moments. GMAP-TD can be directly extended for use with staggered PRT waveforms with minimum modification. The GMAP-TD algorithm provides a computationally tractable and stable clutter filter solution for staggered PRT operation.

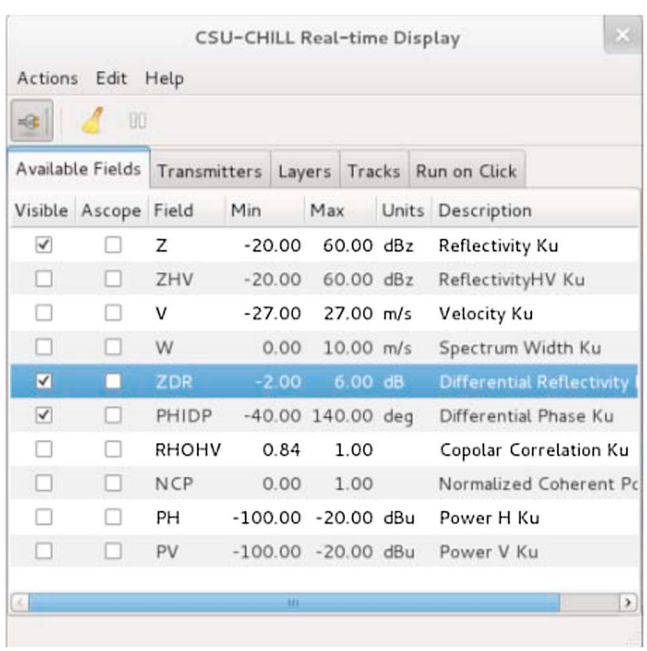

Figure 11. D3R real-time display control panel. Two control panels are provided; one for Ku and one for Ka.

The dual-polarized staggered PRT pulse scheme [*Golestani et al.*, 1995] (please see *Zrnic and Mahapatra* [1985] for the single-polarized version) is used to alleviate the range-velocity ambiguity problem. The maximum unambiguous velocity is determined by $V_a = \frac{\pm\lambda}{4T_u}$. For staggered PRT, $T_u = T_2 - T_1$ with $T_2 > T_1$. For a uniform PRT, $T_u = T$. It is easily shown that for a two-thirds staggered PRT ratio, the unambiguous velocity range is 2.5 times greater than a uniform PRT with the same effective PRT given by $T_e = \frac{(T_1+T_2)}{2}$. The PRT timing modes used on the D3R are shown in Figure 10. Both staggered and

©2014. American Geophysical Union. All Rights Reserved.

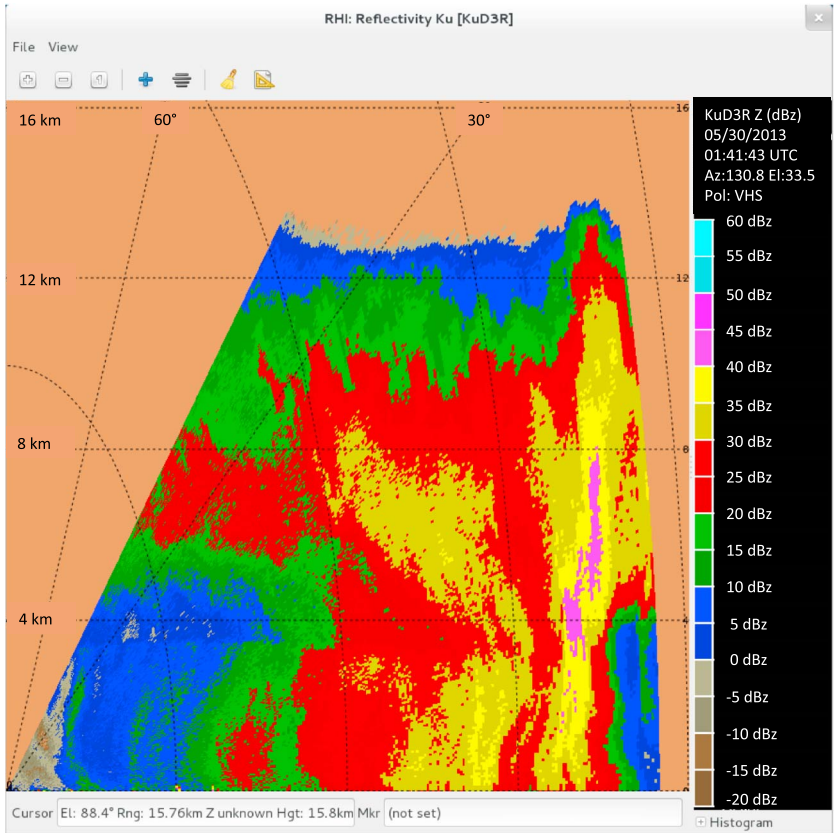

Figure 12. Example real-time display of Ku-band reflectivity for an RHI scan.

uniform PRT pulse schemes are supported. For staggered PRT, a two-thirds timing scheme is used. The alternate transmit simultaneous receive staggered PRT waveform proposed for the D3R is shown in Figure 10.

The D3R's moment processing code dynamically detects the radar operation mode on a ray-by-ray basis. The radar and processing control parameters are fully customizable. The moment processing allows for online calibration and measurements of an internal RF noise source and measurements of the transmit power via the transceiver calibration mechanisms. The online calibration allows for improved accuracy of reflectivity and Z_{dr} by compensating for system variations.

The radar moment data from the moment processor is archived to disk using the Network Common Data Form (NetCDF) 4 format with a D3R-specific data structure. The radar moments and additional radar state information are archived for each processed ray. Each NetCDF file contains a single radar sweep.

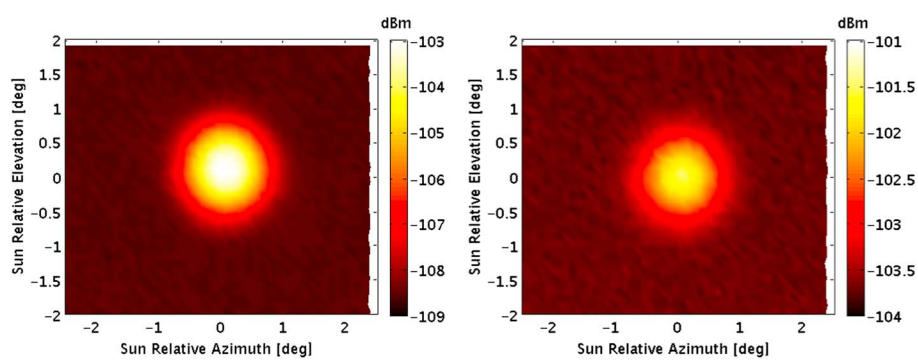

Figure 13. Ku- and Ka-band solar-received power with position relative to the center of the Sun.

©2014. American Geophysical Union. All Rights Reserved.

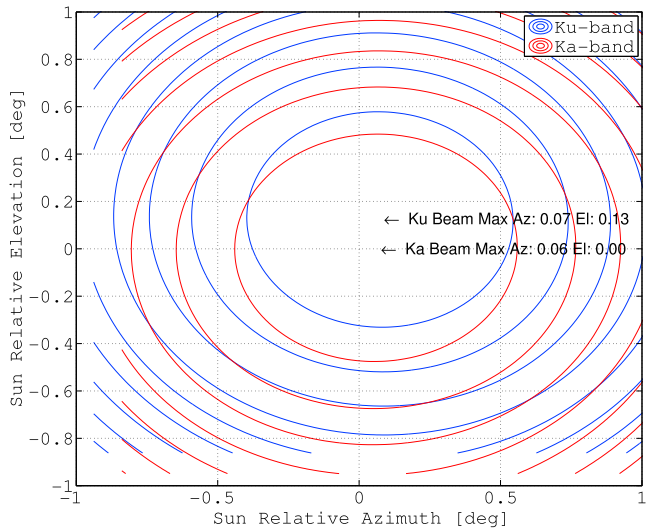

Figure 14. Three decibel contour lines of the five parameter model fitted to the Ku- and Ka-band solar-received power. The azimuth and elevation are relative to the center of the Sun during the scan. This plot provides information on the absolute pedestal position error as well as coalignment of the Ku and Ka antennas.

3.3.4. User Interface

The D3R operation is provided by a user computer that interfaces to the radar control software and data streams through a network connection to the appropriate D3R servers. Scan files can be configured and executed via a command line interface or a graphical user interface. All system control and system status information is similarly accessed. The D3R system status information includes component temperature and voltage monitoring, available data storage capacity, pedestal health and telemetry, AWG and transmitter state, and scan progress. Individual sweeps are grouped into a stack or volume scan. Multiple stacks can be dynamically combined to create ever more complex scan profiles. A scan period can be defined to regularly execute scans at a predefined interval.

The real-time display server, as the name implies, provides a real-time look at the generated radar moments and telemetry. The real-time display provides the radar operator a view of current radar observations. The real-time display provides limited data manipulation, such as data filtering and zooming. An example image of the real-time display software control panel is in Figure 11. The control panel provides a list of available moments to display as well as configuration for the display. Figure 12 is an example of the Ku reflectivity real-time display window available to the radar operator.

4. System Calibration

System calibration is performed and verified on multiple levels depending on the susceptibility to variation and sensitivity of the system's performance to that variation [*Chandrasekar et al.*, 2013]. Electrical and mechanical components undergo parameter variation due to many effects including aging, temperature, humidity, voltage, and environmental contamination. The following subsections describe antenna coalignment verification, absolute reflectivity calibration using a metal sphere, internal transceiver calibration for transmit power variation, and the use of vertically pointing scans to remove Z_{dr} bias.

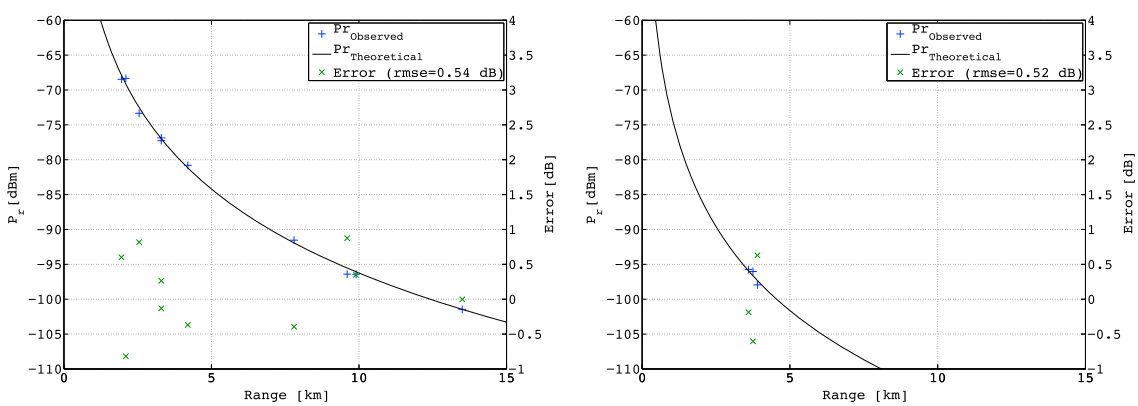

Figure 15. (left) Ku-band and (right) Ka-band sphere calibration from 14 June 2013 starting at 00:00 UTC. The graph shows measured sphere power received and the theoretical receive power curve of a metal sphere of the same diameter. No corrections were made to this data based on calibration results.

©2014. American Geophysical Union. All Rights Reserved.

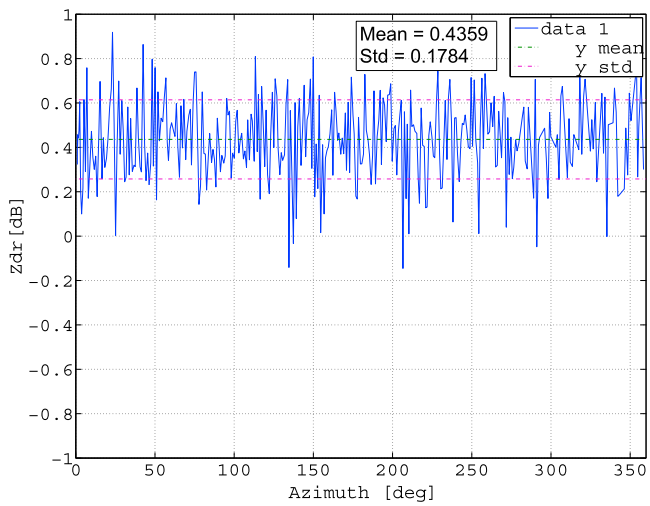

Figure 16. Ku-band short pulse observed Z_{dr} versus azimuth angle on 4 May 2013 at 07:09 UTC during a vertically pointing scan. Z_{dr} observations are from a height of 1.8 km above the radar. The mean $|\rho_{hv}|$ of observation is 0.994. The Z_{dr} mean is 0.4359 dB, and standard deviation is 0.1784 dB.

4.1. Antenna Coalignment

Antenna alignment is determined by the plane of the antenna frame and may be adjusted with shims on four points at the antenna mount points. The coalignment of the Ku and Ka antennas is periodically verified using the Sun as a reference point. This provides a systematic and repeatable method of characterizing and verifying the coalignment of the two antennas. The solar-received power for Ku and Ka as a function of azimuth and elevation relative to the Sun's location are shown in Figure 13. The data from which these images were generated can be used to determine the absolute pedestal position error as well as evaluate the antenna coalignment. Figure 14 shows 3 dB contour lines generated from a second-order polynomial surface fitted to the received power data of Figure 14. The contour lines of the Ku and Ka antennas are shown with respect to the pedestal's position relative to the Sun. Perfect alignment would have the contour lines concentric. It can be noted that during this solar observation from 18 May 2013 at approximately 23:50 UTC, the difference between the coalignment is 0.01° in azimuth and 0.13° in elevation. The bias in the contour's maximum value indicates an absolute pedestal position error.

4.2. Sphere Calibration

Sphere calibration data, performed on 14 June 2013 starting at 00:00 UTC, is shown for both Ku and Ka band in Figure 15. A 25.4 cm (10-inch) metal sphere tethered to a weather balloon filled with helium was released and tracked initially using a theodolite until it was detected and tracked using the real-time displayed reflectivity data. The figures present raw results prior to any corrections being made to account for system reflectivity biases. Therefore, they are purely based on previously measured system parameters and the internal calibration channels. Figure 15 shows the observed power measurements, given the D3R specifications, of a metal sphere of the same diameter to the one launched at various ranges from the radar. The analytically derived expected power observation for a metal sphere of the same diameter is included as a solid curve. A metallic sphere with a diameter, d, in the optical regime ($\lambda << d$) provides a known, constant, isotropic radar cross section that can be used as a system level calibration of the radar. The metal sphere calibration provides a complete end-to-end system calibration for reflectivity [*Bringi and Chandrasekar*, 2001]. Figure 15 shows remarkable agreement with theoretically expected values showing that the radar is well calibrated. The difference

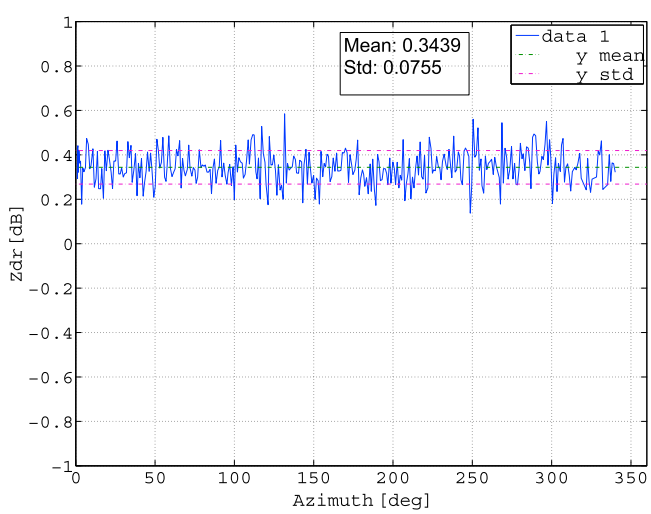

Figure 17. Ka-band short pulse observed Z_{dr} versus azimuth angle on 4 May 2013 at 07:09 UTC during a vertically pointing scan. Z_{dr} observations are from a height of 1.8 km above the radar. The mean $|\rho_{hv}|$ of observation is 0.993. The Z_{dr} mean is 0.3439 dB, and standard deviation is 0.0755 dB.

©2014. American Geophysical Union. All Rights Reserved.

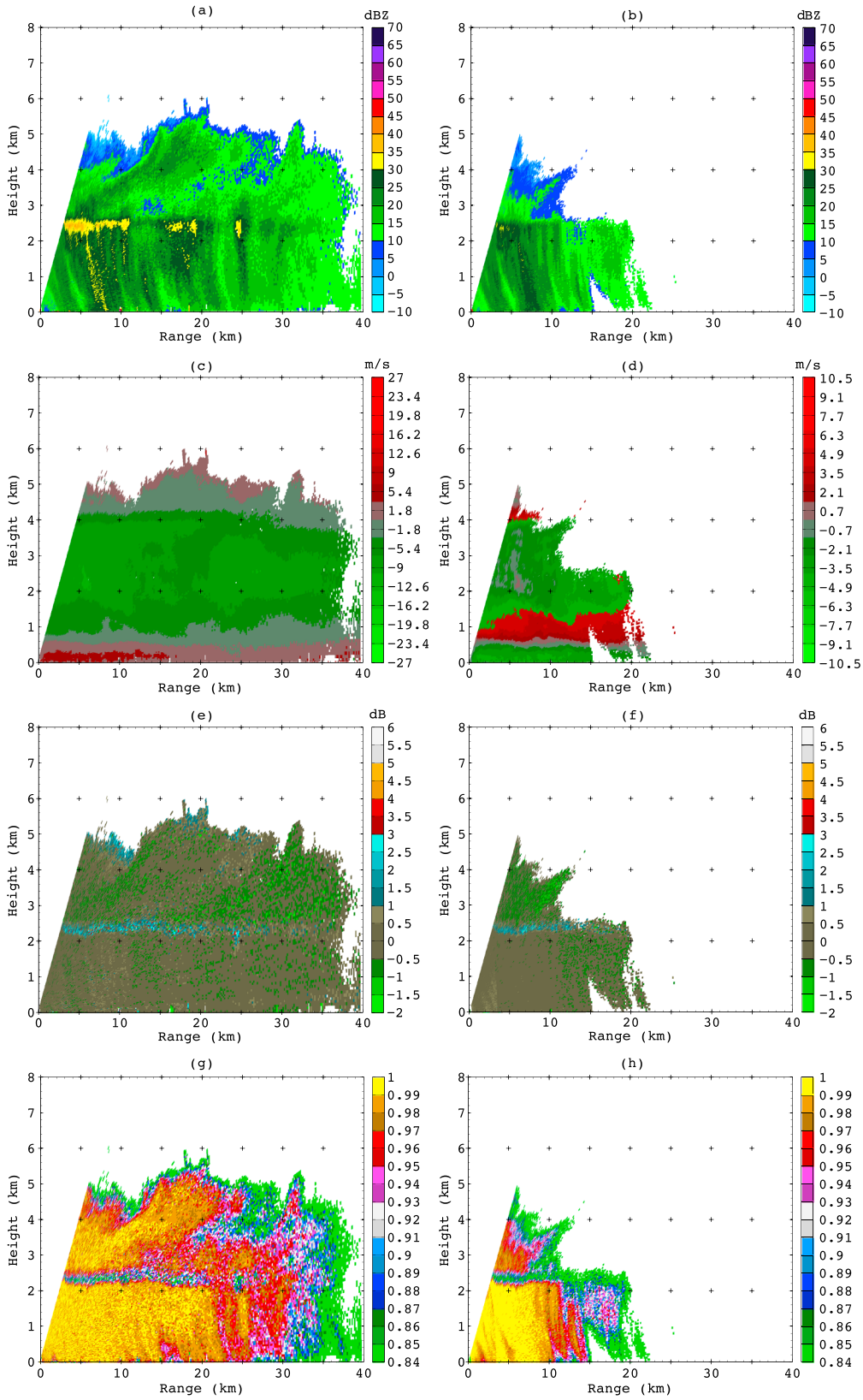

Figure 18. Ku- and Ka-band observations collected on 8 May 2013 at 21:53 UTC. Panels are arranged with Ku-band products on the left column and Ka band on the right column. (a and b) Measured reflectivity's, (c and d) mean Doppler velocities, (e and f) differential reflectivities, and finally, (g and h) the magnitude of the copolar correlation coefficient.

©2014. American Geophysical Union. All Rights Reserved.

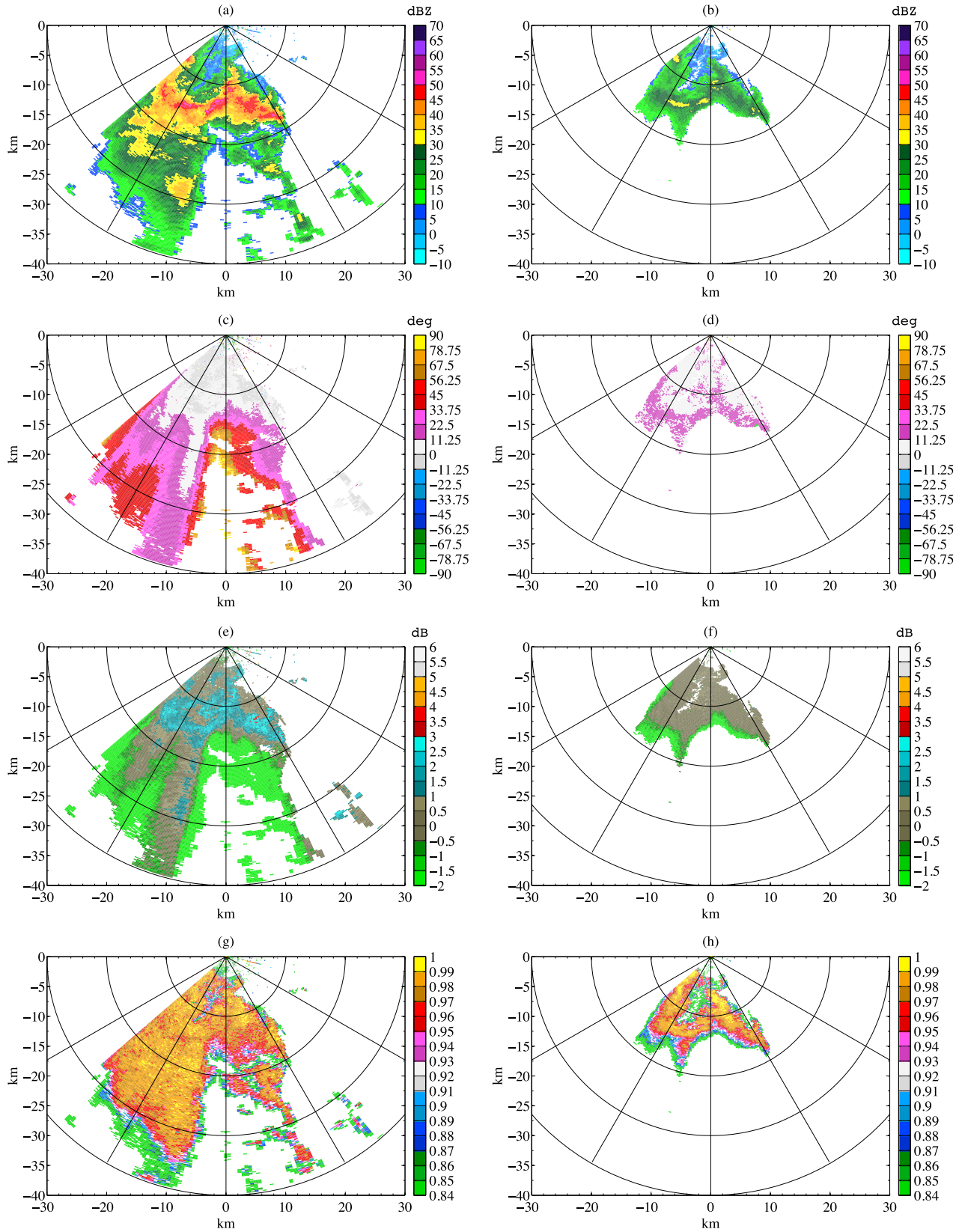

Figure 19. Ku- and Ka-band PPI observations collected on 19 May 2013 at 09:18 UTC of a line of convection. Panels are arranged with Ku-band products on the left column and Ka band on the right column. (a and b) Measured reflectivities, (c and d) differential phase, (e and f) differential reflectivities, and finally, (g and h) the magnitude of the copolar correlation coefficient.

©2014. American Geophysical Union. All Rights Reserved.

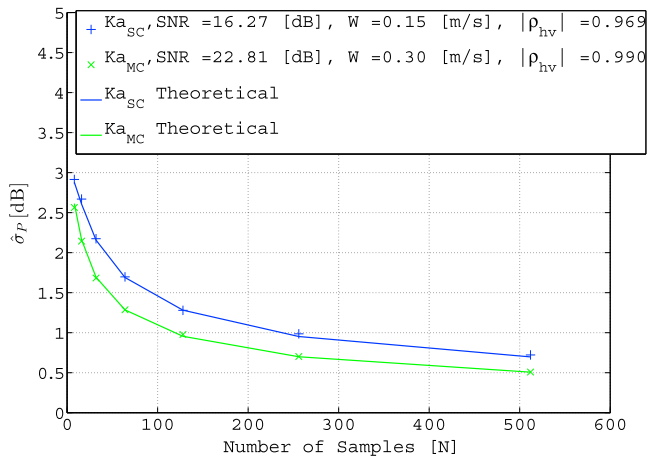

Figure 20. Ka band Z_h standard deviation as a function of integration time for the short-pulse (SC) and medium-pulse (MC) channels.

error is provided on the right side axis and shows that on average, the radar calibration is accurate to within 0.5 dB.

4.3. Transceivers

The transceivers implement a single-pole, double-throw (SPDT) switch to allow the receiver to sample a noise source as well as the transmitted waveform. The transmit power measurements are used to compensate for variations in the SSPAs' power output. Variations in transmit power, if not compensated for, directly impact the accuracy of Z_{dr} as transmit power drift for the H and V polarization channels are not necessarily correlated. The accuracy of reflectivity measurements is similarly affected by variation in transmit power. The implementation of transmit power measurements via the calibration loop also includes gain drift in the receive path. From equation (2), it can be seen that the product of the receiver gain G_r and transmit power P_t are in the numerator of the radar constant equation. Therefore, the measured transmit power, via the calibration loop, appropriately accounts for variation in both receiver gain and transmit power. The remaining parameters in equation (2) are the following: c the speed of light in a vacuum, T_0 the uncompressed pulse width, l_r the receiver finite bandwidth loss, λ the wavelength, G_0 antenna boresight gain, and θ and ϕ the antenna half-power full-width beam widths in their respective planes.

Any Z_{dr} bias introduced by transmit power or receiver gain drift is similarly compensated for using equation (3). The superscripts h and v represent the respective polarization channel and P_{drx} is the received power measured at the digital receiver.

$$C = \left(\frac{cT_0}{2}\right)\left(\frac{G_r}{l_r}\right)\left(\frac{\lambda^2 P_t G_0^2}{(4\pi)^3}\right)\left(\frac{\pi\theta\phi}{8\ln 2}\right) \tag{2}$$

$$Z_{dr} = 10\log_{10}\left(\frac{P^h_{drx}}{P^v_{drx}}\right) - 10\log_{10}\left(\frac{G^h_r P^h_t}{G^v_r P^v_t}\right) \tag{3}$$

An RF noise source is implemented to provide a stable reference for monitoring the receiver gain drift independent of the transmit power measurements. This provides an independent source for validating system health as extreme component parameter drift can be a precursor to component failure.

4.4. Calibration of Polarimetric Variables

The three frequency diverse subpulses used by the D3R have different starting system differential phases. With careful calibration, discontinuities in ϕ_{dp} can be removed when changing from one pulse to the next with range. Alignment of the pulse is accomplished by comparing ϕ_{dp} estimates of two pulses for the same range gate in light to moderate rain. The difference between the estimates can be applied as an offset to one of the pulses and continuity of ϕ_{dp} is ensured. The starting ϕ_{dp} at range 0 can similarly be centered to avoid phase wrapping by applying a fixed offset to all pulses after alignment has been completed.

Z_{dr} is sensitive to system parameter variation between the H and V polarization channels. Absolute Z_{dr} calibration is carried out by performing "bird-bath" scans where the antenna is pointed vertically and rotated in integer multiples of 360° during light precipitation [*Bringi and Chandrasekar*, 2001]. For an unbiased system Z_{dr}, the mean Z_{dr} over the scan should be 0 dB. This method of Z_{dr} calibration is routinely used with example results from 4 May 2013 presented in Figure 16 for Ku and Figure 17 for Ka using the short pulse. A height of 1.8 km is selected for analysis with the mean copolar correlation for the scan at 0.994 for Ku and 0.993 for Ka. For Ku, the mean Z_{dr} for the scan is 0.3459 dB with a standard deviation of 0.1784 dB. Similarly for Ka, the mean of the Z_{dr} observations is 0.3439 dB with a standard deviation 0.0755 dB. The mean Z_{dr} values

©2014. American Geophysical Union. All Rights Reserved.

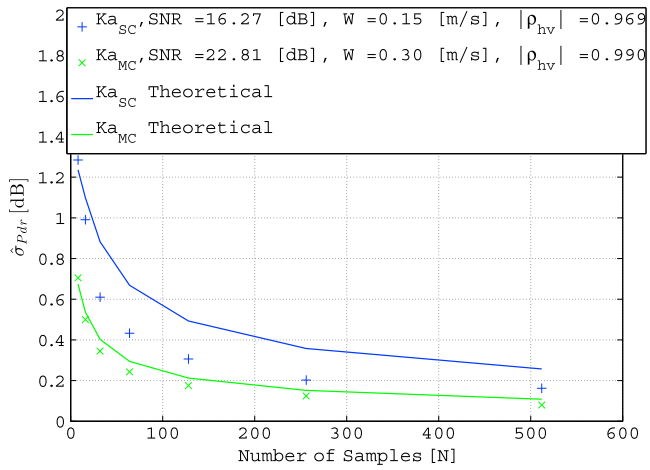

Figure 21. Ka-band Z_{dr} standard deviation as a function of integration time for the short-pulse (SC) and medium-pulse (MC) channels.

determined from the bird-bath scan are then subtracted from future calculation of Z_{dr} to remove any system bias. The Z_{dr} bias for the medium and long pulses are determined in the same way continuity of ϕ_{dp} is maintained. The Z_{dr} bias from the short pulse is used as a reference to correct the medium and long pulse biases at overlapping range gates with light to moderate rain.

5. Sample Observations

The D3R participated in the NASA Iowa Flood Studies ground validation field campaign between 1 May 2013 and 15 June 2013. The field campaign was the first in which the higher power Ka transmitter was deployed in the field. For the sample observations discussed here, the following radar parameters are considered: H-Pol reflectivity (Z_h), differential reflectivity (Z_{dr}), velocity v, spectrum width w, differential phase (ϕ_{dp}), and magnitude of the copolar correlation ($|\rho_{hv}|$). The data presented here are without attenuation correction.

Figure 18 shows Ku- and Ka-band range-height indicator (RHI) observations of stratiform rain on 8 May 2013 at 21:53 UTC. The figure shows eight panel displays of reflectivity, velocity, differential reflectivity, and copolar correlation, respectively. A cursory examination of Figure 18 shows that Ka band returned power falls below the system's noise level after a range of 20 km due to attenuation of the signal from propagation in rain. Additionally $|\rho_{hv}|$, as a function of range, shows a progressive drop off of $|\rho_{hv}|$ below 0.99 as range increases which is indicative of falling signal-to-noise ratio. The purpose of this paper is to show the direct measurements from the radar. Several techniques are available to correct for attenuation as long as the signal is available [*Bringi and Chandrasekar*, 2001]. A detailed examination of attenuation correction is beyond the scope of this paper. Both the Ku and Ka observations distinctly show the melting layer or "bright band." This is easily identified by the increase in reflectivity and decrease in copolar correlation at approximately 2.5 km height. The Ka-band unambiguous velocity range is exceeded, and velocity folding can be observed.

Figure 19 shows Ku- and Ka-band plan position indication (PPI) observation of a line of convection on 19 May 2013 at 09:18 UTC. The eight panel display includes reflectivity, differential reflectivity, differential propagation phase, and copolar correlation coefficient side-by-side for Ku- and Ka-band observations. For both Ku and Ka, the effects of attenuation and differential attenuation are also noticed for ranges beyond points of high reflectivity. The areas of high attenuation correlate to large increases in ϕ_{dp} [*Bringi and Chandrasekar*, 2001]. The range extent over which the signal exists is shorter for Ka band compared to Ku band. This is well known and anticipated. The Ka-band observation for GPM is designed for light rain and snow. Under those operating conditions, the Ka-band observations are available

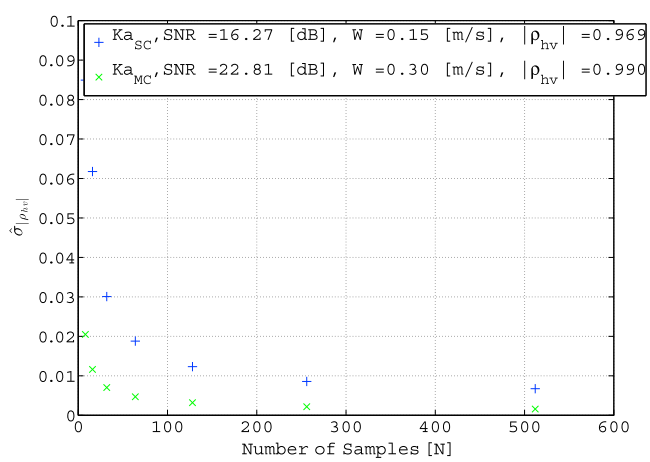

Figure 22. Ka-band $|\rho_{hv}|$ standard deviation as a function of integration time for the short-pulse (SC) and medium-pulse (MC) channels.

©2014. American Geophysical Union. All Rights Reserved.

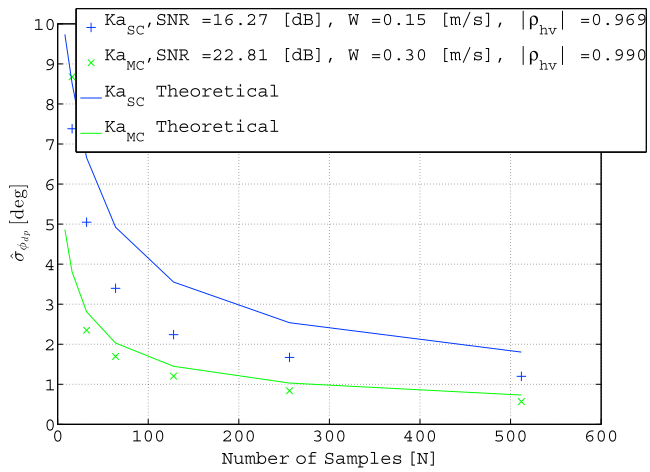

Figure 23. Ka-band ϕ_{dp} standard deviation as a function of integration time for the short-pulse (SC) and medium-pulse (MC) channels.

over the full operational range of the D3R [*Chandrasekar et al.*, 2012].

The quality of products retrieved from radar measurements (e.g., raindrop size distribution, rain rates, and liquid water content) is impacted by uncertainties inherent in the measurements [*Bringi and Chandrasekar*, 2001]. The following section provides quantitative validation of accuracy of Z_h and polarimetric products, namely Z_{dr}, ϕ_{dp}, and $|\rho_{hv}|$. The analysis presented aims to quantify uncertainties associated with the D3R measurements. The analysis consisted of fixed pointing time series data collection for a light-moderate precipitation event. Simultaneous-transmit, simultaneous-receive mode with a staggered PRT of 400 μs/600 μs was used during the collection. The data set was then processed with a varying number of samples (8 through 512 in powers of 2). Uncertainties were estimated by computing the sample standard deviation across rays (at fixed gates with ranges at 2.4 and 3.6 km). Figures 20–23 show the results obtained plotted against the number of samples used. In the case of Z_h, Z_{dr}, and ϕ_{dp}, theoretical values obtained from expressions provided in *Bringi and Chandrasekar* [2001] were also included for reference. Estimates of $|\rho_{hv}|$ and spectrum width using the highest number of samples (512) were used as parameters in the theoretical expressions. Dual-polarization moments are shown as these are sensitive to the performance of both H and V polarization channels. The results indicate that D3R's accuracy of the polarimetric measurements is consistent with theoretical projections.

6. Summary

The dual-frequency, dual-polarization Doppler radar is a key instrument in the GPM ground validation program. The D3R is the analogous dual-frequency ground radar counterpart to the DPR radar on the GPM core satellite. However, in addition to being a dual-frequency radar, the D3R also provides dual-polarization and Doppler capability enabling collection of self-consistent dual-polarization and dual-frequency measurements to assist in the microphysical retrievals and physical validation of GPM observations.

The D3R is meant for extended deployment (on the order of few months) through the United States with potential for overseas operation. Thus, the radar was designed with frequent deployment to remote location in mind. Given the diverse climates covered by GPM, the radar is expected to collect data in all forms of precipitation such as snow and rain, winter and summer, being subjected to a wide range of temperatures and environmental conditions. These scientific and operational demands resulted in a solid-state transmitter design with coaligned antennas.

This paper presented the system architecture and the performance of the D3R. The D3R has already been deployed to numerous locations for field observations including: Northern Colorado, Ontario, Canada, Wallops Island, Virginia, Central Iowa, Western North Carolina. Two of these deployments were in coordination with aircraft, and all deployments were in coordination with other ground instrumentation including radar, rain gauges, and disdrometers. Overall, the D3R has performed very well yielding good scientific observations.

The D3R is calibrated using multiple techniques including absolute calibration using a metal sphere. The alignment of the antennas is checked each time after reassembly for deployment using the solar scan technique. The antennas alignment is consistently repeatable, and alignment holds within 0.1° accuracy.

The standard deviations on the polarimetric measurements were evaluated experimentally by collecting observations of Z_h, Z_{dr}, $|\rho_{hv}|$, and ϕ_{dp}. The standard deviations were compared against theoretical projections, and these compare very well indicating good overall system integrity. The experimental copolar

©2014. American Geophysical Union. All Rights Reserved.

correlation observations in light rain were found to be above 0.99 in the RHI scans of stratiform rain, which again shows the overall system integrity. Data from the D3R have been used in detailed coordinated analysis to make quantitative comparison of Ku- and Ka-band observations by *Duffy et al.* [2013]. Airborne comparison shows excellent cross-validation results with the D3R, demonstrating the quality and usefulness of the D3R observations.

Acknowledgments
This research is supported by the NASA GPM program. The authors are grateful for the early support of Arthur Hou for this project. The authors acknowledge the scientific and operations support from the GPM leadership including Ramesh Kakar, Walt Petersen, and Gail Skofronick Jackson. The radar was developed, assembled, and tested originally at the CSU-CHILL facility; we thank the generous support of the CHILL staff for their assistance. In addition, we would like to thank Nitin Bharadwaj for his contributions to the early development and waveform design, Kumar Vijay Mishra for his early work on the digital receiver, and Ken Hersey for his contributions to antenna pattern characterization and laser tracker coalignment of the antennas. We would like to acknowledge the participation of David Wolff and Walt Petersen in the field programs for all the logistical support. We would also like to acknowledge the help of many others not mentioned here during antenna pattern measurements, integration and testing, field deployments, etc. Finally, we would like to thank the reviewers for their valuable comments and suggestions. The data used for the figures in this work will be made available by contacting the first author.

References

Bharadwaj, N., and V. Chandrasekar (2012), Wideband waveform design principles for solid-state weather radars, *J. Atmos. Oceanic Technol.*, *29*(1), 14–31, doi:10.1175/JTECH-D-11-00030.1.

Bringi, V. N., and V. Chandrasekar (2001), *Polarimetric Doppler Weather Radar: Principles and Applications*, 636 pp., Cambridge Univ. Press, Cambridge, U. K.

Carswell, J., S. Bidwell, and R. Meneghini (2008), A novel solid-state, dual-polarized, dual-wavelength precipitation Doppler radar/radiometer, in *International Geoscience and Remote Sensing Symposium (IGARSS)*, vol. 508, pp. 1014–1017, IEEE International, Boston, Mass.

Chandrasekar, V., and J. Keeler (1993), Antenna pattern analysis and measurements for multiparameter radars, *J. Atmos. Oceanic Technol.*, *10*, 674–683.

Chandrasekar, V., Y.-G. Cho, D. Brunkow, and A. Jayasumana (2005), Virtual CSU-CHILL radar :The VCHILL, *J. Atmos. Oceanic Technol.*, *22*, 979–987.

Chandrasekar, V., et al. (2012), Dual-frequency dual-polarized Doppler radar (D3R) system for GPM ground validation: Update and recent field observations, in *International Geoscience and Remote Sensing Symposium (IGARSS),* pp. 346–349, IEEE, Munich, doi:10.1109/IGARSS.2012.6351567.

Chandrasekar, V., L. Baldini, N. Bharadwaj, and P. Smith (2013), *AMS Short Course on Weather Radar Calibration*, Am. Meteorol. Soc., Boston, Mass.

Duffy, G., S. W. Nesbitt, G. M. McFarquhar, M. Poellot, C. V. Chandrasekar, and D. R. Hudak (2013), In situ microphysical and scattering properties of falling snow in GPM-GCPEx, *AGU Fall Meeting Abstracts*, p. A5.

Durden, S. L., E. Im, F. K. Li, A. Ricketts, A. Tanner, and W. Wilson (1994), ARMAR: An airborne rain-mapping radar, *J. Atmos. Oceanic Technol.*, *11*, 727–737.

Golestani, Y., V. Chandrasekar, and J. Keeler (1995), Dual polarized staggered PRT scheme for weather radars: Analysis and applications, *IEEE Trans. Geosci. Remote Sens.*, *33*(2), 239–246.

Hou, A. Y., G. Skofronick-Jackson, C. D. Kummerow, and J. M. Shepherd (2008), Global precipitation measurement, in *Precipitation: Advances in Measurement, Estimation and Prediction*, edited by S. Michaelides, chap. 6, pp. 131–164, Springer, New York.

Le, M., and V. Chandrasekar (2014), An algorithm for drop-size distribution retrieval from GPM dual-frequency precipitation radar, *IEEE Trans. Geosci. Remote Sens.*, *52*(11), 1–16, doi:10.1109/TGRS.2014.2308475.

Li, L., G. Heymsfield, J. Carswell, D. Schaubert, M. Mclinden, M. Vega, and M. Perrine (2011), Development of the NASA high-altitude imaging wind and rain airborne profiler, in *IEEE Aerospace Conference*, pp. 1–8, IEEE International, Big Sky, Mont.

McLinden, M., P. Siqueira, and N. Majurec (2008), Calibration of the UMass Advanced Multi-Frequency Radar (AMFR), in *International Geoscience and Remote Sensing Symposium (IGARSS)*, pp. 105–108, IEEE International, Boston, Mass.

Meneghini, R., T. Kozu, H. Kumagai, and W. C. Boncyk (1992), A study on rain estimation methods from space using dual-wavelength radar measurements at near-nadir incidence over ocean, *J. Atmos. Oceanic Technol.*, *9*, 364–382.

Moisseev, D. N., and V. Chandrasekar (2007), Nonparametric estimation of raindrop size distributions from dual-polarization radar spectral observations, *J. Atmos. Oceanic Technol.*, *24*(6), 1008–1018, doi:10.1175/JTECH2024.1.

Mudukutore, A., V. Chandrasekar, and E. A. Mueller (1995), The differential phase pattern of the CSU CHILL radar antenna, *J. Atmos. Oceanic Technol.*, *12*(5), 1120–1123.

Mudukutore, A. S., V. Chandrasekar, and R. J. Keeler (1998), Pulse compression for weather radars, *IEEE Trans. Geosci. Remote Sens.*, *36*(1), 125–142.

Nguyen, C., and V. Chandrasekar (2013), Gaussian model adaptive processing in time domain (GMAP-TD) for weather radars, *J. Atmos. Oceanic Technol.*, *30*(11), 2571–2584.

Seto, S., T. Iguchi, and T. Oki (2013), The basic performance of a precipitation retrieval algorithm for the global precipitation measurement mission's single/dual-frequency radar measurements, *IEEE Trans. Geosci. Remote Sens.*, *51*(12), 5239–5251, doi:10.1109/TGRS.2012.2231686.

Siggia, A. D., and R. E. Passarelli (2004), Gaussian model adaptive processing (GMAP) for improved ground clutter cancellation and moment calculation, in *European Conference on Radar in Meteorology and Hydrology*, pp. 67–73, Copernicus, Gottingen, Germany.

Ulaby, F. T., D. G. Long, W. Blackwell, C. Elachi, A. Fung, C. Ruf, K. Sarabandi, H. Zebker, and J. van Zyl (2014), *Microwave Radar and Radiometric Remote Sensing,* chap. 13, 639–641, Univ. of Mich. Press, Ann Arbor.

Vega, M. A., V. Chandrasekar, C. Nguyen, K. V. Mishra, and J. Carswell (2012), Calibration of the NASA dual-frequency, dual-polarized, Doppler radar, in *Geoscience and Remote Sensing Symposium (IGARSS)*, vol. 2, pp. 4625–4628, IEEE International, Munich, Germany.

Wang, Y., V. Chandrasekar, and V. N. Bringi (2006), Characterization and evaluation of hybrid polarization observation of precipitation, *J. Atmos. Oceanic Technol.*, *23*(4), 552–572, doi:10.1175/JTECH1869.1.

Zrnic, D. S., and P. Mahapatra (1985), Two methods of ambiguity resolution in pulse Doppler weather radars, *IEEE Trans. Aerosp. Electron. Syst.*, *4*, 470–483.

©2014. American Geophysical Union. All Rights Reserved.